Theory, observation, and ultrafast response of the hybrid anapole regime in light scattering

Adrià Canós Valero[1], Egor A. Gurvitz[1], Fedor A. Benimetskiy[1], Dmitry A. Pidgayko[1], Anton Samusev[1], Andrey B. Evlyukhin[1,2], Vjaceslavs Bobrovs[3], Dmitrii Redka[3,4], Michael I. Tribelsky[5,6,7], Mohsen Rahmani[8], Khosro Zangeneh Kamali[9], Alexander A. Pavlov[10], Andrey E. Miroshnichenko[11], and Alexander S. Shalin[1,3,12]

[1]ITMO University, Kronverksky prospect 49, 197101, St. Petersburg, Russia

[2]Institute of Quantum Optics, Leibniz Universität Hannover, Welfengarten Street 1, 30167 Hannover, Germany

[3]Riga Technical University, Institute of Telecommunications, Latvia, Riga, Azenes street 12, post code 1048

[4]Electrotechnical University "LETI" (ETU), 5 Prof. Popova Street, Saint Petersburg 197376, Russia

[5]Faculty of Physics, M. V. Lomonosov Moscow State University, Moscow 119991, Russia

[6]National Research Nuclear University, Moscow Engineering Physics Institute, Moscow 115409, Russia

[7]School of Physical Science and Technology & Jiangsu Key Laboratory of Thin Film, Soochow University, Suzhou 215006, China

[8]Advanced Optics and Photonics Laboratory, Department of Engineering, School of Science and Technology, Nottingham Trent University, Nottingham, NG11 8NS, UK

[9]1ARC Centre of Excellence for Transformative Meta-Optical Systems, Research School of Physics, The Australian National University, Canberra ACT 2601, Australia

[10]Institute of Nanotechnology of Microelectronics of the Russian Academy of Sciences (INME RAS), Moscow, Nagatinskaya street, house 16A, building 11

[11]School of Engineering and Information Technology, UNSW Canberra, ACT, 2600, Australia

[12]Kotel'nikov Institute of Radio Engineering and Electronics of Russian Academy of Sciences (Ulyanovsk branch), Goncharova Str.48, Ulyanovsk, Russia, 432000

Abstract. Modern nanophotonics has witnessed the rise of "electric anapoles", destructive interferences of electric dipoles and toroidal electric dipoles, actively exploited to cancel electric dipole radiation from nanoresonators. However, the inherent duality in Maxwell equations suggests the intriguing possibility of "magnetic anapoles", involving a nonradiating composition of a magnetic dipole and a magnetic toroidal dipole. Here, we predict, fabricate, and observe experimentally via a series of dark field spectroscopy measurements a hybrid anapole of mixed electric and magnetic character, with all the dominant multipoles being suppressed by the toroidal terms in a nanocylinder. Remarkably, breaking the spherical symmetry allows us to overlap up to four anapoles stemming from different multipoles with just two tuning parameters. This effect is due to a symmetry-allowed connection between the resonator's multipolar response and its eigenstates. We delve into the physics of such current configurations in the stationary and transient regimes and explore new ultrafast phenomena within sub-picosecond timescales associated with the hybrid anapole dynamics. Based on our theoretical results, we design a non-Huygens metasurface featuring a dual

functionality: perfect transparency in the stationary regime and controllable ultrashort pulse beatings in the transient. Besides offering significant advantages with respect to electric anapoles, hybrid anapoles can also play an essential role in developing the novel field of ultrafast dynamic resonant phenomena.

Introduction

Over the past few years, all-dielectric nanophotonics has become one of the cornerstones of modern research in nano-optics[1,2]. Unlike plasmonic structures, dielectric ones make it possible to overcome the fundamental limitation of Ohmic losses. Utilizing electric and magnetic Mie-like resonances of nanoparticles, consisting of low-loss high-index semiconductor or dielectric materials, such as Si, TiO_2, Ge, GaAs[3,4], enables manipulating both the electric and magnetic components of light at the nanoscale. This emerging field has already led to a wide range of exciting applications, such as low-loss discrete dielectric waveguides[5,6], passive and reconfigurable directional sources[7,8], efficient high harmonic generation mechanisms[9], light-harvesting and antireflective coatings[10–12], all-dielectric metasurfaces with artificially tailored optical response[13–16], dielectric beam deflectors[17], subwavelength all-optical liquid mixing[18], to mention just a few.

The ability to adequately describe and predict electromagnetic scattering is of prime importance to manipulate the behavior of light at the nanoscale. For this purpose, different types of electromagnetic multipole expansions were introduced[19–23]. The charge-current Cartesian decomposition is widely used for describing optical signatures of nano-objects of arbitrary shape[19–21]. One of the most intriguing possibilities delivered by this formalism is the ability to define the so-called toroidal moment family[24–27]. While the well-known electric toroidal dipole moment is associated with the poloidal currents flowing along the meridians of a torus [25], higher-order toroidal moments, also known as mean square radii, feature more complex current distributions recently investigated theoretically in Refs.[28,29].

The electric toroidal dipole is now widely exploited in nanophotonics and metamaterials, active photonics[30], ultrasensitive biosensing[24], and applications requiring strong near-field localization[31,32]. The fields radiated by toroidal moments share the same angular momentum and far-field properties as their electric or magnetic multipolar counterparts, allowing for the realization of two exciting effects: (i) enhanced multipolar response[33] enabled by the constructive interference of the fields, and (ii) mutual cancellation of the far-field contributions via the destructive one, so-called “anapole”[34].

In the aforementioned scenario, an anapole corresponded to a scattering minimum from a given multipole channel[35],[34], leading to a reduction of the overall far-field scattering and confined near-fields[34]. This promising feature has motivated widespread investigations in diverse applications of nanoscale light-matter interactions, such as photocatalysis[36], Raman scattering[37], strong exciton coupling[38], and second and third harmonic generation[39–42].

It should be stressed, however, that while there exists a large amount of literature regarding the stationary (frequency domain) response of the electric dipole anapole (EDA), the number of publications devoted to discussions of transient behavior in the time domain is much fewer. On the other hand, emergent studies point out that the transient regimes may exhibit qualitatively new effects, not observable in the stationary states[43]. In this regard, the understanding and control of the transient response of anapoles is yet to be developed and remains an unexplored realm with potential applications in the novel field of ultrafast dynamic resonant phenomena[43,44].

Furthermore, the vast majority of the investigations on EDAs are limited to the electric dipole term only[45–48]. Despite the observation of high order EDAs in Ge and Si nanodisks[49], no experimental works have proven the existence of magnetic anapoles. If the magnetic anapoles do exist, their spectral overlap with electric ones should give rise to the enhanced radiation suppression and lead to unprecedently concentration and confinement of the electromagnetic energy within the scattering particle. In turn, this effect should provide new exciting degrees of freedom for designing light-matter interactions. Until now, this issue has remained a challenging task since the formation of the so-called 'hybrid anapoles (HA)' requires a careful overlap of electric and magnetic multipoles with their toroidal counterparts. Indeed, magnetic toroidal moments themselves have only been discussed in a very recent work, where a complex cluster of nanodisks was necessary to induce the desired multipole response[50].

Importantly, spherically symmetric structures are unable to exhibit HAs[51,52] since the latter always remain hidden by the contributions of other multipole moments with non-negligible scattering. Nevertheless, recent developments in the theory of multipole expansions[20,29] have opened the possibility to qualitatively and quantitatively investigate higher-order electric and magnetic anapoles in scatterers with arbitrary shape, beyond the limitations of the quasistatic regime.

Here, for the first time we design and demonstrate experimentally the existence of such exotic current configurations, schematically illustrated in **Figure 1**a. In the stationary regime, making use of our recently developed multipolar formalism[53], we show how anapoles come into being, arising from multipoles of alternate electric and magnetic origin, linked in scatterers with broken spherical symmetry. This feature makes it possible to spectrally overlap up to four anapoles varying just two geometrical parameters of the proposed resonator.

We show that the counterintuitive opportunity to satisfy *four* anapole conditions varying only *two* parameters is strongly related to the violation of the scatterer's spherical symmetry, playing a key role in our study. As a result, the four conditions become non-independent. The latter is clearly shown by treating the problem in terms of open cavity modes, i.e. quasi-normal modes [54,55](QNMs, depicted in **Figure 1**a). The expansion of the fields on a basis of QNMs demonstrates that the overlap of four anapoles occurs owing to the superposition of just *two* fundamental QNMs supported by the structure.

Physically, the overlap gives rise to the excitation of a 'super' dark anapole with strongly minimized scattering, accompanied by an extremely effective electromagnetic energy concentration within the scatterer (achieving an order of magnitude enhancement with respect to the EDA), resulting in highly confined near-fields. The performed analysis also provides a complete physical picture of the effect, establishing general theoretical guidelines valid for anapoles of arbitrary order and their combinations, in scatterers of arbitrary shape.

The HA originates from the far-field destructive interference of *all* the leading electric and magnetic Cartesian multipoles of a finite cylindrical scatterer with their associated toroidal moments. For the first time, higher-order (quadrupolar) toroidal moments are shown to contribute to essential features of the scattering response of an isolated high-index nanoparticle. We validate our results by fabricating a series of individual silicon nanocylinders supporting the HA and confirm its existence experimentally via dark-field spectroscopy measurements.

The discussion is further extended to envision future applications of our effect in the novel field of ultrafast resonant phenomena. We predict and theoretically describe the unconventional temporal dynamics of the HA nanoresonator under a pulse with a sharp temporal cutoff. The analysis shows the emission of two ultrashort energy 'flashes'[56] at the leading and trailing edges

of the excitation and the formation of coherent beating oscillations[57] in the scattered electric field.

It should be stressed that contrarily to the conventional EDA, the HA preserves its nonradiating nature in the presence of any dielectric substrate. The QNM formalism allows us to unveil the physical mechanism behind such a counterintuitive effect, and further demonstrate its breakdown in the transient regime. The spatiotemporal maps reveal relevant changes in the beating pattern of the decaying modes, explicitly dependent on the substrate refractive index.

Finally, based on the developed theoretical description, we design and demonstrate a dual-functional metasurface consisting of an array of HA particles combining full transparency in the stationary regime and a highly tunable spatiotemporal response in the transient one.

The Cartesian multipole expansion and high-order anapole conditions

The analysis of a nanoparticle's optical response is usually carried out via the decomposition of the scattering cross section as a sum of multipoles, which represent independent scattering channels of the object. Here we utilize the irreducible Cartesian multipole expansion derived in Ref.[29] (for completeness, also given in the Supporting Information S1), which explicitly considers higher-order toroidal moments. The latter interpretation is our starting point towards the physical understanding of higher-order anapoles.

Within this approach, an electric or magnetic anapole of order *n* in a subwavelength scatterer is given by the condition:

$$P^{(e,m)}_{i_1\ldots i_n} + i\frac{k_d}{v_d}T^{(e,m)}_{i_1\ldots i_n} = 0 \qquad (1)$$

Here we have denoted n th order electric or magnetic moments with $P^{(e)}$ and $P^{(m)}$, and the corresponding electric and magnetic toroidal moments with $T^{(e)}$ and $T^{(m)}$, respectively. The number of subscripts indicates each Cartesian tensor's order, i.e., one subscript corresponds to a dipole, two correspond to a quadrupole, etc. k_d, ε_d are the wavenumber and the dielectric permittivity of the host medium, and v_d is the speed of light in the medium. In the previous we have chosen to depart from the usual terminology employed for denoting toroidal moments, which refers to the $T^{(e)}$ as simply 'toroidal', to clearly differentiate between toroidal moments contributing to radiation of the 'electric' type, and those contributing to radiation of the 'magnetic' type. Their physical origin is also different[29]: the $T^{(e)}$ originate from poloidal currents, while the $T^{(m)}$ arise due to circulating magnetic fields. We also clarify that in order to minimize the number of involved terms[22], the coordinate origin for the multipole expansion has been set to the particle center of mass.

The HA occurs when more than one multipole moment fulfills Eq.(1) at a given wavelength, resulting in a simultaneous suppression of scattering of two or more channels. However, as mentioned above, light, in general, can be radiated out through other non-zero multipole moments, destroying the overall effect. Thus, only the cancellation of all the leading multipoles can enable a true HA.

For the sake of clarity, in the rest of the manuscript, we will rely on the widespread notation for low-order multipoles, i.e. p, m for electric and magnetic dipoles, and $Q^{(e)}$, $Q^{(m)}$ for electric and magnetic quadrupoles.

Results

Observation and multipole analysis of HAs

Under conventional plane wave illumination, hybrid anapoles of homogeneous spherical particles are hidden by the contributions of other multipoles [51,58]. We will show that this restriction naturally vanishes for nano-objects with additional geometrical degrees of freedom, like finite cylinders or parallelepipeds. We will unveil the fundamental reason behind this unusual behavior throughout this work.

Let us consider a cylindrical silicon nanoparticle in the air. Starting now, we will use amorphous silicon (a-Si) in both theoretical and experimental studies (for details refer to the Supporting Information S13). The illumination scheme is presented in the left inset of **Figure 1**b (normally incident x-polarized plane wave propagating along $-z$-direction).

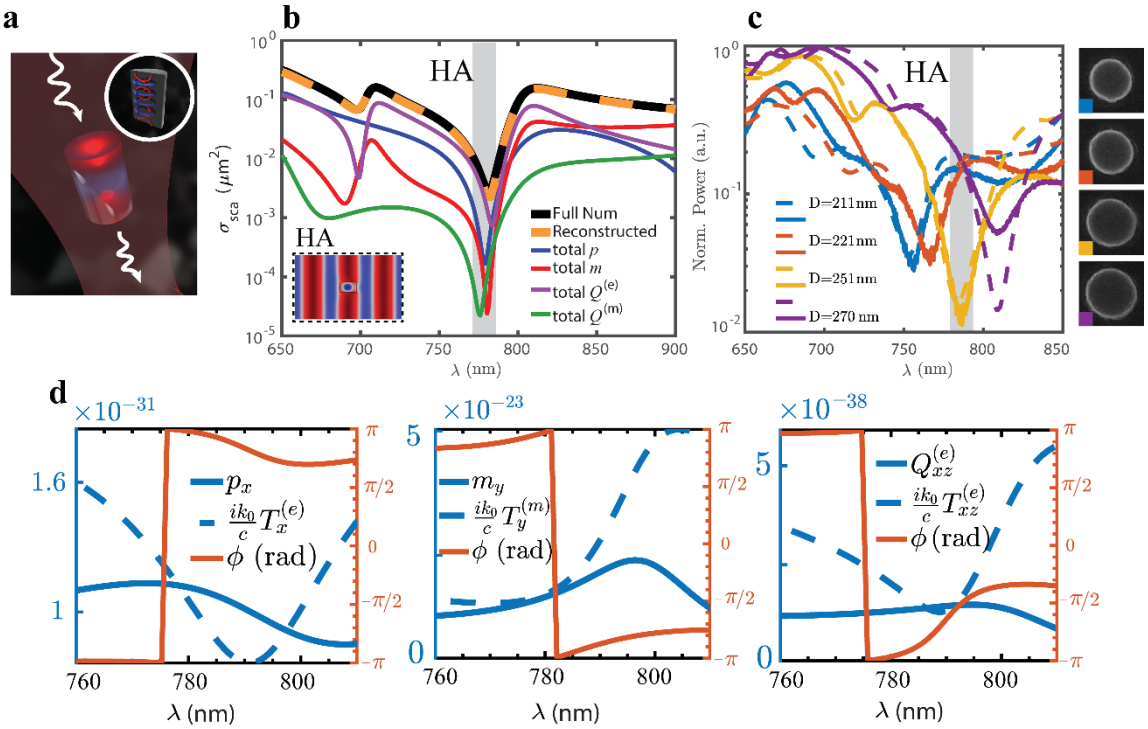

Figure 1. (a) Artistic representation of the novel effect. A normally incident plane wave excites nontrivial modal contributions in a Si nanocylinder whose interference with the background field leads to a four-fold hybrid anapole yielding the nanoantenna virtually invisible in the far-field, with localized near-field. Inset depicts the two resonant eigenmodes' current distributions arising due to standing waves between the top and bottom walls (red) and lateral walls (blue) in the vertical plane. (b) Multipole reconstruction of the numerically obtained scattering cross section for the cylindrical amorphous silicon nanoparticle. In the legend caption, "total" implies that both basic and toroidal contributions of a given multipole are plotted. The inset corresponds to the x-component of the electric field. The cylinder's geometrical parameters are height H=367 nm and diameter D=252 nm. Point HA ($\lambda = 782$ nm) corresponds to the minima of the HA. (c) The colored regions indicate the left plot: measured (solid lines) and simulated (dashed lines) scattering spectra of single isolated nanocylinders with different diameters D. The spectral positions of the hybrid anapoles. Right plot: SEM micrographs of the corresponding nanocylinder samples. The colored edges in each micrograph are associated with the measurements' legend entries. (d) Amplitudes and phase differences between the multipoles and their toroidal counterparts. Panels from left to right, respectively: the basic electric and electric toroidal dipoles, the basic magnetic and magnetic toroidal dipoles, and the basic electric and electric toroidal quadrupoles. Amplitudes correspond to the left ordinate-axis, and phase differences are read from the right ordinate-axis.

The design methodology is based on the following: We note that the spectral positions of the full (basic together with toroidal contributions), electric dipole and magnetic quadrupole anapoles are

mainly dependent on the cylinder's radius. In contrast, the wavelengths of the full magnetic dipole and electric quadrupole anapoles change both as functions of the cylinder height and radius. **Figure S2** in the Supporting Information illustrates the spectral behavior of the multipolar anapoles with variations of the geometrical parameters in detail. Thus, carefully tuning these two geometrical degrees of freedom makes it possible to place the anapoles of all the leading terms ultimately close to each other (**Figure 1**b), providing a strong scattering minimum (**Figure 1**b-c, point HA).

The total scattering cross section and its multipole decomposition after the numerical optimization are shown in **Figure 1**b. Good agreement between the sum of the multipole contributions given by Eq.(S1) in the Supporting Information and the result of the full-wave simulations in Comsol Multiphysics is demonstrated, proving that only the first four multipoles are sufficient to fully describe the optical response of the nanocylinder in the visible range. Therefore, the low-scattering regime renders it perfectly dark to the incident radiation (see the inset on **Figure 1**b).

The different panels in **Figure 1**d show the amplitudes and phase differences of the three most relevant multipoles with their toroidal moments. The results further confirm that the generalized anapole condition in Eq.(1) is well fulfilled for each pair (the amplitudes are equal, and they are π rad out of phase) at the hybrid anapole wavelength $\lambda = 782$ nm. Particularly, this implies that we have succeeded in exciting, for the first time, quadrupole anapole moments in the visible range. Here we recognize that owing to the presence of polarization losses of the dielectric, the cancellation of the electric quadrupole is not as pronounced as in a lossless structure (see Supporting Information S17).

To confirm our theoretical predictions on the hybrid anapole, we have carried out direct scattering spectroscopy measurements for a set of standalone nanocylinders with tailored dimensions in the optical spectral range (**Figure 1**c). The measured scattering spectra (solid lines, **Figure 1**c) exhibit a pronounced dip, shifting with the increase of the nanocylinder diameter D, in excellent agreement with the calculations (dashed lines, **Figure 1**c). Technical details on the fabrication and the optical measurement setup can be found in the Supporting Information S14. While an increase of the nanocylinder's lateral size leads to an overall redshift of the multipole anapoles, they almost perfectly overlap at $D = 251$ nm, where the most pronounced HA results in a large drop in scattering efficiency, of almost two orders of magnitude, rendering the nanocylinder virtually invisible. We note that the other dips indicated in the measured spectra also correspond to HAs, although their overlap is not as much pronounced, but still results in a significant scattering reduction.

The near-zero values of the full scattering coefficients do not imply the induced polarization currents in the particle to be also close to zero. This is in agreement with the usual anapole behavior[59], but due to the suppression of several multipoles simultaneously, the hybrid anapole also displays much better confined internal fields. **Figure 3**b demonstrates the volume-averaged electromagnetic energy density inside the cylinder at the hybrid anapole wavelength to exceed nine times the value of free space almost without leakage of the field outside the particle volume. In its turn, the latter further reduces the interaction with the surrounding (see the following sections).

New perspectives offered by individual HA nanoresonators

Both HAs and EDAs are characterized by suppressing far-field radiation while displaying enhanced near-fields. This naturally poses the question of whether HAs can present any uncommon features and/or fundamental advantages with respect to EDAs for nanophotonics applications. To answer this question in detail, **Figure 2** shows the internal field distributions and multipole moments associated with the conventional nanodisks supporting EDAs, commonly

employed in nanophotonic designs, in comparison with the HA. The near and far-field characteristics of EDAs are currently well understood in terms of the destructive interference of the electric dipole and electric toroidal dipole excitations within the nanoresonator[34], whose peculiar signature can be appreciated from the poloidal-like field distributions arising within the nanoparticle (see **Figure 2a**). However, the multipole decomposition of the scattering spectra reveals that while the electric dipole radiation can be significantly suppressed, EDAs display nonnegligible contributions of the magnetic quadrupole to radiation[34]. This corresponds to a fundamental limitation of the EDA design, since modes of resonators with inversion symmetry in the z-direction will always radiate as combinations of multipoles possessing even or odd parity[60,61], and can only be overcome with careful tuning of the incident beam profile[62].

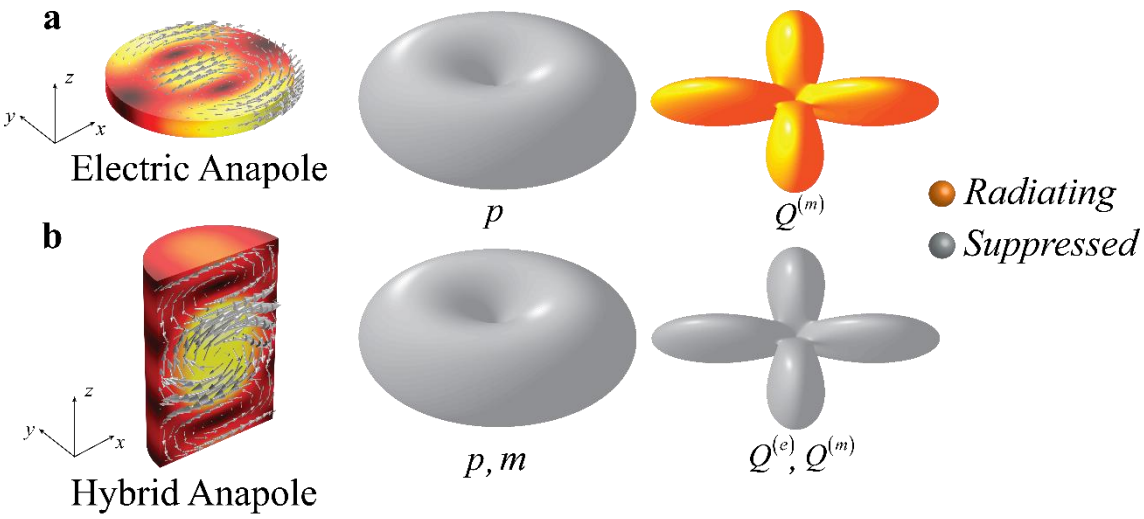

Figure 2. Near and far-field characteristics of electric and hybrid anapoles. (a) From left to right: the normalized intensity of the internal electric field in the electric anapole nanodisk, and corresponding vector field (gray arrows). Angular pattern of the multipoles radiated and suppressed by the EDA. The two designs are obtained by fixing the refractive index $n = 3.87$. The considered EDA is obtained at $kR = 1.795$, $R/H = 5$, similar to Refs.[40,63]. (b) Same as in (a), for the HA, with $kR = 1$, $R/H = 1/3$.

Conversely, the complex mixture of electric and magnetic multipole moments giving rise to the HA leads to an internal field distribution unlike the EDA (**Figure 2b**). It hinders a straightforward interpretation of the near-fields in terms of Cartesian multipoles, which already points at a different physical origin. As illustrated in **Figure 2b**, and shown quantitatively in **Figure 1b**, the HA allows to simultaneously suppress the electric and magnetic dipoles and quadrupoles under plane wave illumination. Here we must clarify that with the term 'suppression' we refer to the appearance of strong local minima in the spectra of each multipole channel. The effect is clearly appreciable when comparing the scattering cross sections of the two structures (**Figure 3a**); despite that the total volume of the nanoresonator is almost ten times larger than the EDA nanodisk, the scattering intensity for the HA is found to be more than ten times weaker and can be considered broadband.

Interestingly, this fact does not decrease the Local Density of Optical States (LDOS), as demonstrated by the calculations of the total electromagnetic energy stored within the two structures (**Figure 3b**). The energy stored at the HA nanoresonator surpasses that of the EDA by more than an order of magnitude, which promises essential benefits for boosting light-matter interactions and enhance nonlinear effects. The stored energy is also significantly higher than that of the recently observed 2nd order EDAs[40,63], (a quantitative comparison between EDAs, 2nd

order EDAs and HAs is provided in section S4 of the Supporting Information). Finally, it can be seen that the modes supporting the HA display significantly larger quality factors than the EDA.

Overall, the numerical studies carried out in this section provide conclusive evidence on the superiority of HAs with respect to EDAs as nonradiating sources capable of enhancing light-matter interactions at the nanoscale. A more thorough understanding of the effect is thus desirable as a means to properly design future applications.

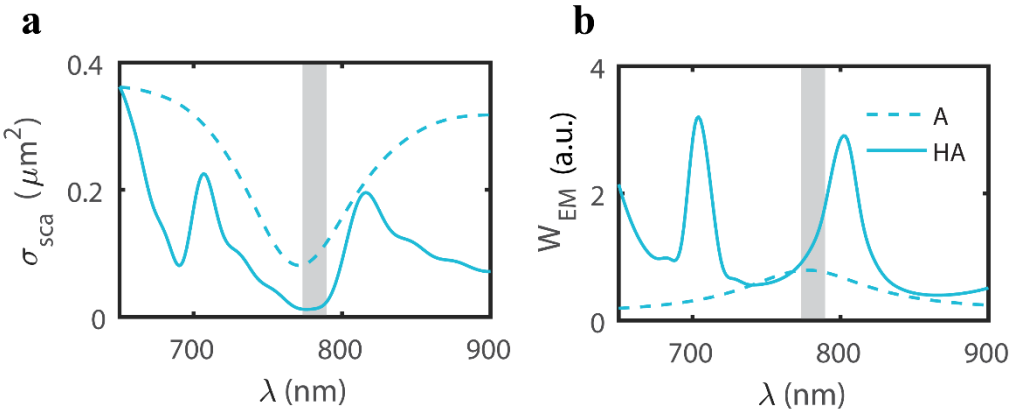

Figure 3. Radiated power (a), and stored electromagnetic energy (b), at the electric anapole (indicated by A) and the hybrid anapole (denoted with HA). The geometrical parameters are the same as in **Figure 2**. The grey band in the plots indicates the spectral position corresponding to the destructive interference between the electric dipole and the electric toroidal dipole giving rise to the EDA. Despite having a volume around ten times larger than EDAs, the hybrid anapole's radiation suppression is an order of magnitude more efficient and can be considered broadband. Contrarily, the total stored electromagnetic energy is enhanced by more than an order of magnitude. In (b), the electromagnetic energy has been normalized on 10^{-30} J to facilitate the interpretation.

Intrinsic modal content of the hybrid anapole

While Cartesian multipoles are suitable for the description of far-fields, in this section we employ the natural QNM expansion[55] of near-fields and internal currents, which in the following will allow us to unveil the physics behind the HA further. QNMs provide a suitable basis for the induced polarization currents, which can then be expanded according to:

$$\mathbf{J}(\omega,\mathbf{r}) = \sum_{\mu} \alpha_{\mu}(\omega)\tilde{\mathbf{J}}_{\mu}(\omega,\mathbf{r}) - i\omega\delta\varepsilon\mathbf{E}_{inc}(\omega,\mathbf{r}). \qquad (2)$$

Here $\tilde{\mathbf{J}}_{\mu}(\mathbf{r}) = -i\omega\delta\varepsilon\tilde{\mathbf{E}}_{\mu}(\mathbf{r})$, $\alpha_{\mu}(\omega)$ and $\delta\varepsilon$ are, respectively, the induced modal scattering current distribution as a function of the internal mode field, the excitation coefficient of the mode μ describing its contribution to the total current at a given frequency, and the permittivity contrast with the host environment.

We use a modified version of the freeware MAN developed by the authors of Ref.[54]. More details on the approach can be found in the Supporting Information S5, S6. For simplicity, we consider a dispersionless, lossless nanocylinder with a constant refractive index $n \approx 3.87$ (corresponding to aSi at 780 nm), so that the excitation coefficients depend solely on the fields of an individual QNM[54]. Losses and refractive index dispersion of the original design are negligible in the considered spectral range (see Supporting Information S12). Therefore, this approximation does not significantly change the scattering cross section and average electromagnetic energy density.

The QNM expansion results are displayed in the different panels of **Figure 2**. The correctness of our calculations in the studied spectral range, particularly near the scattering dip, is well validated in **Figures 2**a-b by comparing the sum of the individual QNM contributions with the numerically obtained total scattering cross section (a) and average electromagnetic energy density inside the cylinder (b). From here on, we shall label the QNMs with the standardized notation for the modes of isolated cylindrical cavities[64], i.e. $(TE,TM)_{uv\ell}$, where the sub-indices denote the number of standing wave maxima in the azimuthal (u), radial (v), and axial (ℓ) directions. TE and TM indicate the predominant nature of the internal field distribution. Specifically, TM (transverse magnetic) modes have $H_z \approx 0$, while TE (transverse electric) have $E_z \approx 0$.

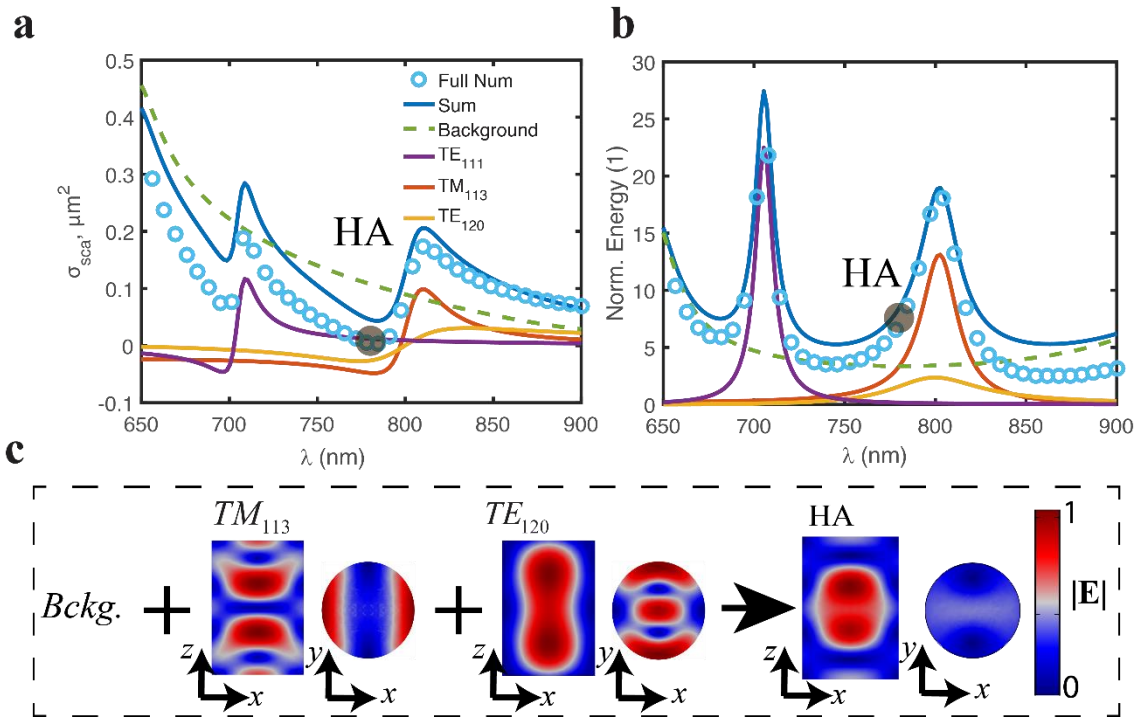

Figure 4. (a) Alternative scattering cross section decomposition using the QNM expansion method. The full-wave simulation is nearly the same (without losses), as in **Figure 4**, but linearly. Colored lines are the individual contributions of the physical QNMs. The contributions of modes having their resonances outside the considered spectral range are added up in the green dashed line. The resonant modes in the considered spectral range are associated with the TE_{111}, TE_{120}, and TM_{113} modes of an isolated cylinder. The blue line corresponds to the reconstructed scattering cross section, confirming that all the resonant spectral features can be successfully recovered via this method, and demonstrating good agreement near the hybrid anapole, point HA. (b) Spectra of the volume-averaged electromagnetic field energy inside the cylinder and the excited modes (see Supporting Information S15, for a numerical justification of the latter decomposition). Colors and legends are the same as in (a). The electromagnetic energy density has been normalized with respect to the incident electromagnetic energy density in the vacuum $w_{EM} = \varepsilon_0 E_0^2$. Excellent agreement is obtained with the full-wave simulations. (c) Normalized internal electric field distributions of the two most relevant modal contributions near point A, from left to right, associated with Fabry-Perot (TM_{113}) and Mie-like (TE_{120}) standing wave patterns (TE_{111} is very weak near the hybrid anapole), respectively. Their addition via Eq. (2), together with the background modes (Bckg.), leads to the reconstruction of the internal fields of the hybrid anapole, also displayed on the right-hand side of (c). All the electric fields have been normalized with their respective maxima, to enhance their visualization.

The spectral behavior of each resonant QNM is described by a Fano lineshape[65], (see Supporting Information, S6). The other nearby QNMs constitute the background scattering contribution of the particle.

In **Figure 4**a we note that a total of three QNMs resonate in the visible range. The correct reconstruction of the scattering cross section requires considering background modes, despite their resonances being outside the considered spectral range (green dashed line). Nevertheless, only the TM_{113} and TE_{120} modes present a 'Fano-like' response at point HA.

The pronounced low scattering regime can be easily grasped as a consequence of modal interference: a clear sign that this is indeed the case are the resonant negative contributions to scattering presented by both the TE_{120} and TM_{113} modes. It implies that, when the incident field impinges in the resonator, energy exchange takes place between the two and the background QNM fields[66]. This owes to the fact that the QNMs do not obey the usual conjugate inner product relation of orthogonal modes in Hermitian systems[67]. It is important to emphasize the unusual feature of the hybrid anapole: the two resonant QNMs dominating the spectra are *simultaneously negatively suppressed* by interference with the background. For comparison, the QNM decomposition of a conventional dipole anapole disk is given in the Supporting Information S7.

A completely different picture arises within the resonator. **Figure 4**b presents the modal decomposition of the internal energy stored in the cylinder in the vicinity of point HA. This is one of the main results of the section. Contrarily to the multipole expansion, the QNM decomposition allows us to distinguish the eigenmodes' contributions to the internal fields clearly. Firstly, we observe a significant enhancement of the electromagnetic energy (around nine times), with respect to the incident plane wave. Secondly, it is clearly seen that the stored energy at the hybrid anapole is mainly driven by the TM_{113} mode due to its higher quality factor and the proximity of its resonant wavelength to the hybrid anapole wavelength, in a minor measure by the TE_{120} and the sum of the background contributions. Overall, the QNM analysis given in **Figure 4** demonstrates that both the invisibility effect (outside the cylinder) and the internal energy enhancement at the HA are mediated by the simultaneous resonant response of the TM_{113} and the TE_{120} modes. On the other hand, the background modes, while they do not apparently define the spectral features of the figures of merit, also play an important role since their interference with the resonant ones gives rise to the invisibility effect. This interpretation is consistent with early investigations regarding the formation of Fano lineshapes' in the scattering cross section of spherical resonators[58].

The electric field distributions of the TE_{120} and TM_{113} modes are shown in **Figure 4**c. Following Refs.[68,69] we can classify the first as a 'Mie' type mode, similar to the ones supported by an infinite cylinder, while the second is of the 'Fabry-Perot' (FP) type [68], arising due to the formation of a standing wave pattern between the top and bottom walls of the resonator, i.e. having non-zero axial wavenumber ($\ell \geq 1$). Their distinct origin unveils the reason why it is possible to obtain a HA in this particular geometry, contrarily to spherical scatterers. As shown in the Supporting Information S8, the real parts of the eigenwavelengths of the modes in the cylinder can be estimated as[70]

$$\lambda_{uv\ell} \approx \frac{\pi D}{n_p \sqrt{\left(\frac{\ell\pi}{2}\frac{D}{H}\right)^2 + z_{uv}^2}}, \tag{3}$$

where z_{uv} is the vth root of the uth Bessel function of the first kind for *TE* modes, or its first derivative for *TM* modes. For FP modes, $\ell \neq 0$ and the denominator in Eq. (3) displays a strong dependence on the cylinder's aspect ratio D/H . In contrast, since $\ell = 0$ for Mie modes, their eigenwavelengths only change with D. Thus, the eigenwavelengths and the multipolar content of these two mode types *are independently tunable*, resulting in a flexible control over the resonator's optical response and enabling the simultaneous scattering suppression observed in **Figure 1**a-b, and **Figure 4**a -the hybrid anapole.

A straightforward comparison between the QNM and multipolar methods allows determining the multipoles radiated by a given QNM (see the Supporting Information S9). Specifically, Figure S5 leads us to conclude that the TE_{120} mode emits primarily as p, with a minor $Q^{(m)}$. In contrast, the TM_{113} mode scatters as a combination of m and $Q^{(e)}$ (in both cases, referring to both their basic and toroidal counterparts). When scattering from a mode is resonantly suppressed, radiation from the multipoles associated with it is also strongly minimized, and results in the different multipole anapoles observed in the decomposed spectra of **Figure 4**a. Thus, the close proximity of the destructive interference points of the TE_{120} and TM_{113} modes at point HA leads to an overlap of the anapoles of the four dominant multipoles. In this fashion, using the QNM expansion approach, we have shown an alternative and general physical explanation of dark scattering regimes and qualitatively illustrated its link to the particle's multipolar response. This self-consistent approach will further be effectively applied to understand the physics behind the particle-substrate interaction.

As a final remark, we point out that the quality factors of the TE_{120} structure's and TM_{113} modes are, respectively, 12 and 33. A direct comparison with the TE_{120} supporting a conventional anapole disk (see Supporting Information S7) shows that the mode's quality factor at the hybrid anapole is more than four times larger, confirming the earlier discussion of **Figure 3**b. Therefore, we anticipate the much better performance of the hybrid anapole for *second and third harmonic generation* processes with respect to conventional anapole disks, since nonlinear scattering cross sections scale linearly with the quality factors of the modes involved[71].

Hidden mechanism inducing the preservation of the HA for an arbitrary dielectric substrate

We will now illustrate a novel effect in detail, unique to the hybrid anapole, by which its nonradiating nature can be preserved in the stationary regime when deposited on any dielectric substrate. The underlying mechanism will be harnessed in the following sections to modulate the transient response of the isolated nanocylinder.

In comparison with any other scattering phenomena including conventional anapoles, the hybrid anapole is remarkably robust in the presence of a substrate. This particular behavior is illustrated in **Figure 5**a, where we have plotted the calculated scattering cross sections of the cylinder in free space and deposited over glass ($n_s = 1.5$), hypothetical substrates with $n_s = 2, 3$ and over amorphous silicon ($n_s = 3.87$). The amplitude and spectral position of the scattering dip are almost undisplaced from the free-space values while the refractive index contrast at the bottom of the particle remains non-zero. However, we observe drastic changes in the Fano profile's shape, once the contrast is absent (silicon particle over silicon substrate). There is a nontrivial underlying mechanism by which the hybrid anapole is “protected” against modifications of the substrate refractive index. The physics becomes transparent when examining the distinct nature of the two resonant modes involved in forming the HA (**Figure 5**c). On the one hand, increasing the substrate's refractive index leads to a decrease in the lower wall reflectivity, which is crucial for

the standing Fabry-Perot mode TM_{113} inside the resonator, while approaching n_s at the particle's refractive index results in a higher energy leak towards the substrate and a substantial decrease in the quality factor Q_ℓ . Consequently, the resonance flattens and disappears when the lower boundary becomes transparent, as shown in **Figure 5**b.

The standing wave pattern of the TM_{113} resembles a one-dimensional Fabry-Perot cavity on a dielectric substrate. The QNMs of this simplified model have the advantage of being analytically solvable[55], thus providing valuable physical insight easy to extrapolate to the problem at hand. As we derive in the Supporting Information S11, the QNMs are formed by two interfering plane waves traveling in opposite directions inside the cavity, when the driving wavelength satisfies the condition

$$r_{21}r_{23}w^2 = 1, \tag{4}$$

where $w = \exp(ik_\ell n_r H)$ and r_{21}, r_{23} are the Fresnel reflection coefficients from the cavity-air and the cavity-substrate interfaces, respectively. The quality factor of a QNM with axial index ℓ is calculated as

$$Q_\ell = -\frac{\ell\pi}{\ln\left(r_{23}r_{21}\right)}. \tag{5}$$

Equation (5) serves very well to illustrate the substrate influence on the TM_{113} mode. When the two reflection coefficients are unity, the energy is completely stored inside the resonator and Q_ℓ is infinite. Similarly, a decrease in the substrate reflection coefficient leads to radiative losses and a decrease in the quality factor, effectively becoming zero when the contrast is absent. Indeed, a lower quality factor leads to less appreciable spectral features, as observed in the simulations (**Figure 5**b). Another important conclusion can be drawn from the expression of the eigenfrequency ν_ℓ, given by (see Supporting Information S11) :

$$\nu_\ell = \frac{c\ell}{2n_p H} + i\frac{c}{4\pi n_p H}\ln\left(r_{23}r_{21}\right). \tag{6}$$

The real part of the resonant wavelength of the QNM is independent of the refractive index at the walls. Thus, modifying n_s does not shift the spectral position of the resonance (i.e. does not shift the hybrid anapole wavelength), but simply changes the amplitude and width of the Fano profile.

With proper normalization, and employing the notation of the inset in **Figure 5**b, the amplitudes of the incoming and outgoing plane waves inside the resonator are $\left|A_2^+\right| = \sqrt{\alpha r_{12} w}$ and $\left|A_2^-\right| = \sqrt{\alpha r_{23} w}$, with $\alpha = 1/\left(4H\varepsilon\right)$ (see Supporting Information S11 for details). Plane waves reflected from the substrate are thus decreased with decreasing index contrast. Consequently, the same occurs with the lower field maxima of the TM_{113}. While this prediction is observed in the simulations for relatively low contrasts, the behavior at minimal differences is very different (see the case $n_s = 3$ in **Figure 5**c). In the latter situation, the standing waves along z become negligible compared to the initially weaker standing waves in the x-y plane, and the QNM can only be well described numerically.

Contrarily, it is noteworthy that even comparably small contrast (3 – 3.87) leads to enough contribution of the TE_{120} mode to preserve the scattering dip still (see **Figure 5**b). This second

mode's standing wave pattern develops in the lateral walls of the cylinder, and therefore depends much less on variations of the reflectivity of the lower wall, keeping an almost constant quality factor (see Supporting information S10). Most of the QNM energy is then stored in the resonator even in the case of zero effective contrast with the substrate, as demonstrated in **Figure 5**c. It results in a larger contribution of the TE_{120} mode to extinction at small contrasts, and a decrease of radiation from the electric quadrupole and magnetic dipole. The hybrid anapole is now mainly driven by electric dipole radiation stemming from the TE_{120} mode (see **Figure S6**b in the Supporting Information). Thus, for large n_s the hybrid anapole *degenerates into a conventional electric dipole anapole*, but still retains its non-radiative nature, since the other multipoles become negligible due to the small reflections at the lower wall of the nanocylinder.

Characteristics and substrate-mediated modulations of the temporal dynamics of HAs

The QNM theoretical framework is highly suited for quantitative investigations of nanoresonator dynamics under ultrashort pulses[54]. While challenging to explore, the effects taking place at the scale of tens of fs are gradually becoming experimentally accessible[72,73]. They can result in counterintuitive phenomena challenging to interpret in terms of the multipolar machinery commonly utilized to design the optical response of nanoresonators under continuous wave (CW) illumination.

The study of the temporal dynamics of Fano resonances arising in different photonic systems has been gaining increasing interest recently[44,57,74] since the knowledge of both the spatial and temporal structure of the scattered field can enable a more comprehensive understanding of its interaction with matter[75] under ultrashort pulses. Among the novel, promising effects, Fano resonances have been shown to display ultrafast energy spikes when illuminated by a pulse with sharp variation[75]. Such energy spikes were tentatively associated with the rapid breakdown of the balance between the high and low Q modes whose mutual destructive interference leads to the Fano profile under CW illumination.

While the spikes were predicted in infinite cylindrical scatterers, here we anticipate for the first time their occurrence in a realistic structure in the optical regime. Simultaneously, the coherent interplay between the TE_{120}, TM_{113} and the background modes induce beating. While this second effect might not seem remarkable at first glance, it opens the possibility to realize *ultrafast time modulation of the scattered signal* in the transient regime.

To investigate the system's time dynamics, we initially perform a series of numerical experiments (see **Figure 5**d-g). In the simulations shown in **Figure 5**d-g, the hybrid anapole nanoparticle is excited by a plane wave square pulse with duration $\tau = 400\,\text{fs}$, (see inset in **Figure 5**d) sufficiently long to observe both stationary and transient regimes. The scattered power is then plotted in **Figure 5**d, and a more detailed view of the transient after the pulse is shown in **Figure 5**e for different refractive index contrasts with the substrate. In all cases, sharp energy spikes occur right after the pulse shut-off. However, the number and shape of the peaks are different for each scenario. Remarkably, regardless of the substrate index, the radiated power in the stationary regime remains negligible due to the mechanism described above. The HA thus behaves very differently in the stationary and transient regimes; while being nonradiative in the stationary regime for any dielectric substrate, in the transient, it emits energy spikes that can be controlled with the underlying substrate.

The latter behavior is also reflected on the recorded spatiotemporal maps of the E_x field in **Figures 5**f-g, where the characteristics of the system's beating can be fully grasped. Interestingly,

contrary to the conventional Fano resonance[57], we observe the formation of several beatings at the trailing edge of the pulse.

We note that, unlike in Ref.[76] for our system, it would be incorrect to trace an analogy with a two-level quantum system to describe the time dynamics, since the optical response of the structure is driven by several eigenmodes (several QNMs). We investigate the system's modal dynamics in detail by calculating the QNM contributions to the scattered field in the time domain via a Fast Fourier Transform algorithm, following Ref. [54]. The scattered field at any point in space can then be written as $\mathbf{E}_{sca}(\mathbf{r},t)=\sum_{\mu}A_{\mu}(t)\tilde{\mathbf{E}}_{\mu}(\mathbf{r})$, where $A_{\mu}(t)$ is the contribution of mode labeled with μ (see specifics in Supporting Information S16). The calculations demonstrate that, despite the broader content of Fourier harmonics contained in the square pulse, the transient effects at the start and end of the latter are mediated by the same QNMs responsible for the HA in the CW regime (see **Figure S11**).

At high contrasts, the TM_{113} mode leaks from the resonator, and a well-defined beating pattern is observed. The beating is even along the x-axis, reflecting the symmetry of the fields of the dominant modes. At lower contrast, the decreased contribution of the TM_{113} leads to exponential damping, a clear sign of the predominance of a single resonant mode.

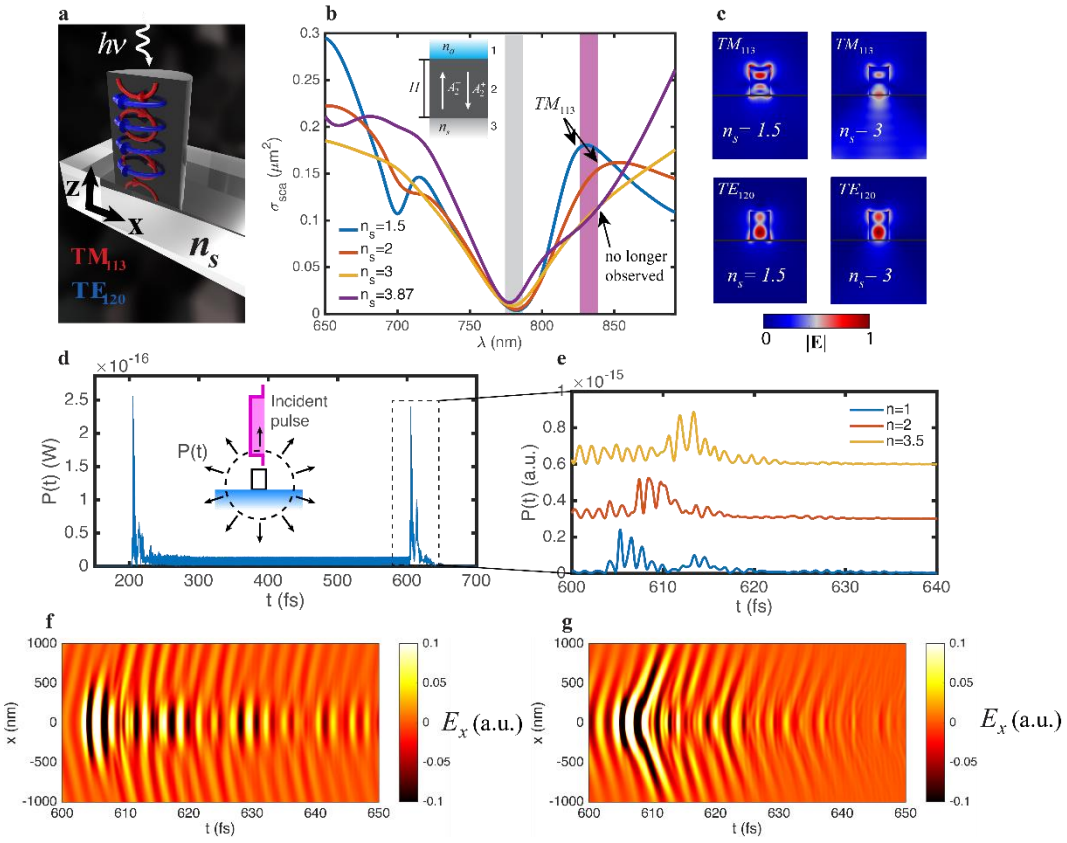

Figure 5. Stationary and transient response of the hybrid anapole with different index contrasts with the substrate. (a) Scheme depicting the setup and the excited eigenmodes. (b) Comparison between the numerically obtained scattering cross sections for the nanocylinder with the size from **Figure 1**, deposited on substrates with increasing refractive index. The calculations are performed with the full experimental aSi refractive index given in the Supporting Information S13. Inset of (b): One-dimensional Fabry Perot model of the TM_{113} mode. (c) xz field distributions of the QNMs TE_{120} and TM_{113} when the cylinder is

deposited over substrates with the different refractive index. As predicted by our theory, losses from the TM_{113} mode increase when decreasing the refractive index contrast. Contrarily, the TE_{120} mode remains confined in the scatterer. (d-f): Temporal response of the hybrid anapole under a plane wave square pulse injected at 200 fs with a duration of 400 fs; (d) Scattered power as a function of time; (e) Different beating patterns of the decaying eigenmodes after the plane wave excitation as a function of n_s ; (f-g) Spatiotemporal maps of the x-component of the scattered electric field measured along the x axis for $n_s = 1$ (f) and $n_s = 2$ (g), measured from the beginning of the modal decay. The color bars are saturated for better visualization.

To gain insight into the mechanism responsible for the energy spikes, we develop a simple approach to calculate the QNM decomposition of the instantaneous power radiated by the nanoresonator, given by:

$$P(t) = \int_{\partial V^+} \left[\sum_{\mu} A_{\mu}(t) \mathbf{E}_{\mu}(\mathbf{r}) \right] \times \left[\sum_{\mu} A_{\mu}(t) \mathbf{H}_{\mu}(\mathbf{r}) \right] \cdot d\mathbf{S} , \tag{7}$$

The integral runs over the resonator's external boundary ∂V^+. Eq. (7) is quite general and can be applied to calculate $P(t)$ from an arbitrary nanoresonator embedded in an arbitrary non-absorptive, passive environment and illuminated by an arbitrary pulse. The derivation is given in section S16 of the Supporting Information. We first reconstruct $P(t)$ with Eq.(7), with a basis of 50 QNMs, obtaining good agreement with FDTD simulations (**Figure 6**a-b). A mismatch is observed in the amplitude of the two energy spikes, but the calculation successfully reproduces the main features of the transient effects. We attribute the mismatch to a reduced QNM basis and the strong dependence on the finite-element mesh utilized to calculate the modal fields. However, the underlying mechanisms are better understood with a simplified model with three QNMs, corresponding to the resonant TE_{120} and TM_{113}, together with a single background mode. A comparison of this model with the basis with 50 QNMs (including discretized modes of the continuum, so-called PML modes[55,77]) is given in **Figure S13** of the Supporting Information.

Interestingly, Eq.(7) features interference terms between different QNMs of the form $\int_{\partial V^+} A_{\mu}(t) A_{\nu}(t) \mathbf{E}_{\mu}(\mathbf{r}) \times \mathbf{H}_{\nu}(\mathbf{r}) \cdot d\mathbf{S}$, which play an important role, as shown in **Figure 6**c (green curve). In the stationary regime, the interference between the TM_{113} and the background mode results in a negative contribution to the radiated power. On the other hand, the direct terms contribute positively, and the addition of the two results in smaller scattering (destructive interference), in analogy with the classical interpretation with toroidal moments. When the incident pulse is shut-off at 600 fs, the direct terms start decaying exponentially, but the interference terms abruptly become positive. Since the QNMs responsible for the interference terms have very different eigenfrequencies, beating is induced, and as a result, two positive energy peaks appear in the spectra.

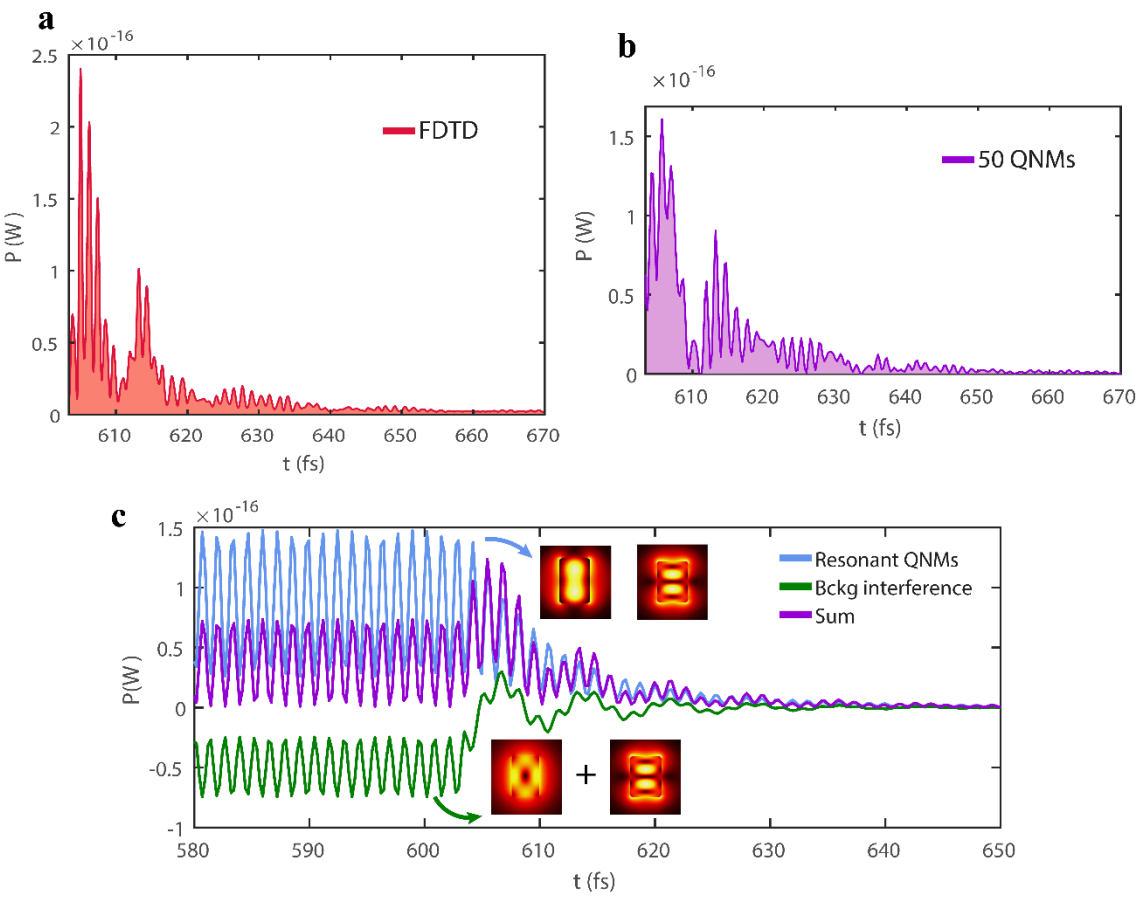

Figure 6. Modal decomposition of the radiated power as a function of time. (a) FDTD calculations of the radiated power in the transient, for the pulse depicted in **Figure 5**d. (In all the calculations, the cylinder is in the air). (b) reconstruction of the radiated power with 50 QNMs. (c) Reduced QNM model with only 3 QNMs (their normalized electric field norms) also allows reproducing all the essential physics of the system dynamics. The curve captioned 'Bckg interference' includes the cross terms between a background mode, identifiable as the well-known magnetic dipole mode[78], and the resonant TM_{113} mode. The curve captioned 'Resonant QNMs' consists of the direct terms of the TM_{113} and TE_{120} modes. 'Sum' corresponds to the addition of the direct and interference terms. The colored arrows indicate which QNMs have been used to calculate each curve.

We note that the interference terms in vacuum are mainly driven by the interaction of the TM_{113} mode with the background. However, as shown in **Figure 5**b, the TE_{120} mode increases its overall contribution to scattering when the index contrast with the substrate decreases. A controlled variation of the substrate index can therefore modify the modal content, and consequently modify the number, shape, and amplitude of the energy spikes.

Non-Huygens transparent metasurface with controllable transients

The potential that transient modulation offers can be fully exploited in practice by fabricating metasurfaces inheriting (and enhancing), the single-particle mechanism described in the previous section.

In particular, the HA can be harnessed to design fully transmissive, all-dielectric metasurfaces without relying on the well-known Huygens condition[7,79], and simultaneously realize controllable ultrafast switching by harnessing transients (see **Figure 5**a-d). Contrarily to the latter,

the light traverses the structure without significant phase variation, thus rendering the metasurface invisible (see shadowed selection in **Figure 7**b). This is a direct consequence of Eq.(1). It can be easily seen by writing the transmission coefficient as a sum of the relevant multipole contributions of the meta-atoms[80]:

$$t = 1 + t_p + t_m + t_{Q^{(m)}} + t_{Q^{(e)}} \tag{8}$$

Each term in the previous sum is proportional to the corresponding total multipole moment (basic and toroidal contributions).

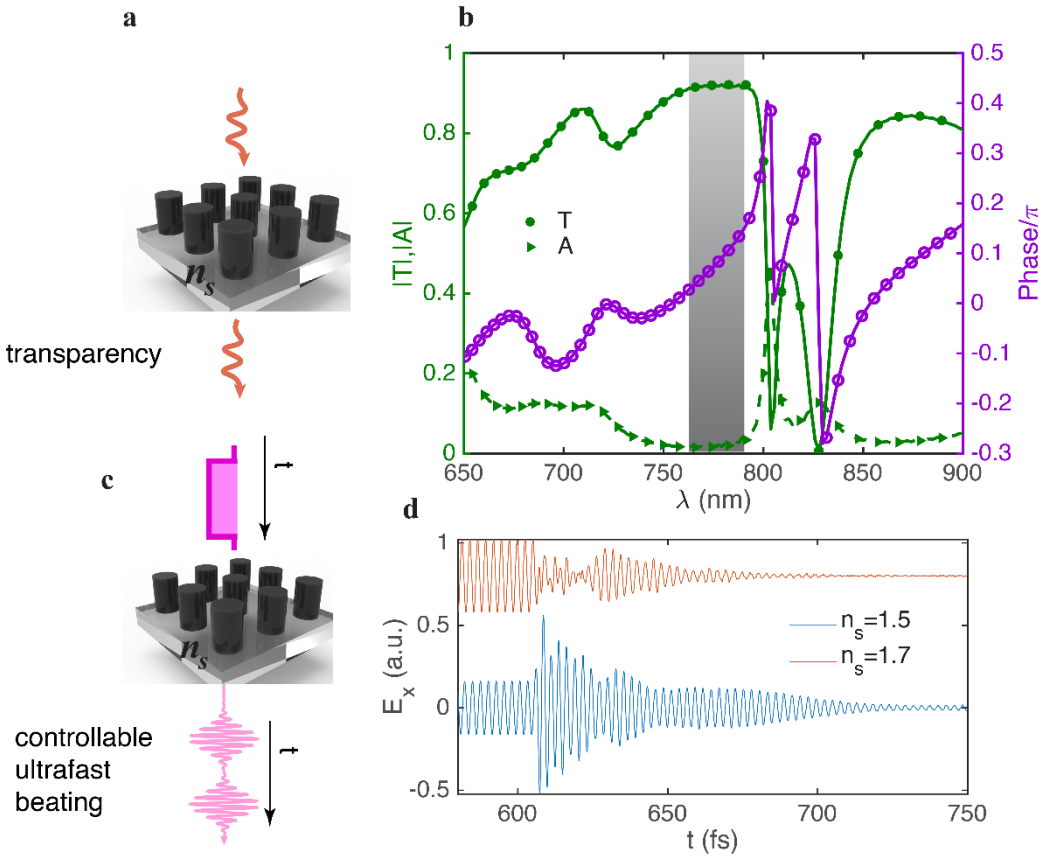

Figure 7. Design of a subwavelength hybrid anapole-based metasurface, featuring dual functionality in the stationary and ultrafast regimes. The period is set to 530 nm. (a) artistic representation of the proposed metasurface operating at the hybrid anapole in the stationary regime. The structure is illuminated by an x-polarized plane wave, passing through the array completely undistorted. (b) Transmission, absorption, and phase of the transmitted wave with respect to the incident one. As predicted by Eqs. (1) and (8), the out-of-phase basic and toroidal moments induce a transparency band with minimal phase perturbation (shaded region). The calculations have been performed in the presence of a substrate with $n_s = 1.5$. (c) Artistic representation illustrating the metasurface response in the sub-ps regime, when excited by a plane wave pulse. (d) E_x component of the scattered field from the metasurface as a function of time at the end of the plane wave pulse, for $n_s = 1.5$ and after increasing the substrate index by 0.2. The results demonstrate that transient oscillations of the metasurface are highly sensitive to changes in the substrate index, opening a pathway towards tunable ultrafast beating.

When Eq. (1) is fulfilled, the multipolar contributions in Eq. (8) are zero. Consequently, we are left with $t \approx 1$ in Eq. (8), and the incident wave leaves the system unperturbed (see **Figure 7**a).

This condition is closely fulfilled in a transmission band around the hybrid anapole wavelength ($\lambda = 782\,\mathrm{nm}$ as previously), as indicated in **Figure 7**b. Polarization losses induce absorption, which slightly decreases transmission. The considered period (530 nm) is not unique, i.e. once the geometry supporting the hybrid anapole for an isolated particle is known, a subwavelength metasurface of such particles will mimic the single-particle behavior far away from the first diffraction order[81].

In analogy with the single-particle behavior, the metasurface induces ultrafast beating of the scattered field in the transients at the beginning and the end of a plane wave pulse (see **Figures 7**c-d). Remarkably, however, the sensitivity to the contrast with the underlying substrate is significantly accentuated, inducing large changes in the modulated scattered signal with an increase of n_s of only 0.2, as can also be observed in the supplementary video, where the complete picture on the evolution of the near-field topology as a function of time is presented.

The sub-ps relaxation times of the metasurface, together with the high sensitivity of the transients to the substrate index opens an exciting pathway towards the spatiotemporal control of ultrafast dynamic effects. Among the interesting perspectives, ultrashort laser pulses can be effectively modulated in time by tailoring the transient phenomena. The high substrate sensitivity can be exploited to dynamically tune the transient response of the metasurface in different temporal regimes by selecting the appropriate modulation technology[82]. The bulk refractive index of the substrate can be tuned, for example, using phase-change materials such a GeTe[83] using temperature as a control parameter. More sophisticated, yet much faster refractive index changes could be achieved by tuning optical nonlinearities arising in the substrate as a function of the incident beam intensity (e.g. if ITO constitutes the underlying substrate[84]). Finally, modifying the free electron density in the substrate with electrical gating[85] might be a promising approach to achieve the desired tunability in practical applications.

Discussion

In the stationary regime, we have theoretically predicted and experimentally confirmed the existence of hybrid anapoles, previously unnoticed non-scattering regimes requiring the simultaneous destructive interference of electric and magnetic cartesian multipoles with their toroidal counterparts. Remarkably, only two design parameters are necessary to spectrally overlap four multipole anapoles. This counterintuitive behavior is explained by a careful analysis of the eigenmodes, which confirms that breaking the spherical symmetry leads to additional conditions linking the electric and magnetic anapoles to the same QNM. For the first time, quadrupole anapoles and magnetic anapoles have been confirmed experimentally in isolated subwavelength nanoparticles. To broaden our knowledge of anapole electrodynamics beyond the electric dipole approximation, we have developed a solid physical picture regarding the fundamental eigenmodes driving the resonator response. Magnetic anapoles and quadrupole anapoles display field confinements several times larger than electric anapoles, promising higher enhancements of nonlinearities in the absence of linear scattering. In section S18 of the Supporting Information, we also demonstrate the possibility to obtain the HA regime under illumination by a focused Gaussian beam possessing orbital angular momentum. Theoretically, the HA, unlike a conventional nanoantenna, should not experience any torque nor net force, an ‘unmovable’ object. This could open interesting opportunities for optical manipulation.

In the transient regime, the prior analysis has allowed us to design at will the breakdown of the hybrid anapole conditions to obtain ultrafast modulation of the scattered power. The present theory shows that efficient spatiotemporal control of the transients mediated by the underlying substrate can be achieved while maintaining scattering in the stationary regime at the vanishing

level. Following the established theoretical guidelines, we propose and verify numerically a non-Huygens, subwavelength metasurface obeying the same principles and therefore featuring a double functionality: (i) substrate-independent full transparency in both amplitude and phase mediated by the hybrid anapole in the stationary regime, and (ii) ultrafast, substrate-dependent signal modulation in the transient regime, mediated by its breakdown. The necessary changes in the substrate refractive index to observe appreciable modifications of the transient response of the metasurface are well in the range of available technologies for dynamic tuning[83], drastically expanding the available degrees of freedom.

Therefore, combining our findings with up-to-date modulation techniques holds great promise for future applications in the emerging field of ultrafast dynamic nanophotonics. Remarkably, the ultrashort scattering peaks arising at the transient can be used to enhance ultrafast nonlinearities[74] (e.g. single-particle lasing) or coded in terms of their intensity as a function of the substrate index to realize light-based computing[86].

Finally, the proposed non-Huygens metasurface can enable the temporal/spectral shaping of fs laser pulses by interfering the latter with the outgoing scattered signal.

Acknowledgements

The research reported in this publication was supported by the Russian Foundation for Basic Research (Project No. 20-02-00086, 20-52-00031), the Moscow Engineering Physics Institute Academic Excellence Project (agreement with the Ministry of Education and Science of the Russian Federation of 27 August 2013, Project No. 02.a03.21.0005) for the modeling of the resonant light scattering and computer simulation. The contribution of the Russian Science Foundation for the time-domain calculations (Project No. 21-12-00151) and the provision of user facilities (Project No. 19-72-30012) is also acknowledged. A.B.E acknowledges the support from the Deutsche Forschungsgemeinschaft (DFG, German Research Foundation) within the Cluster of Excellence PhoenixD (EXC 2122, Project ID 390833453).

References

[1] S. M. Kamali, E. Arbabi, A. Arbabi, and A. Faraon, *Nanophotonics* **7**, 1041–1068 (2018).

[2] M. L. Brongersma, *Nanophotonics* **10**, 643–654 (2020).

[3] D. G. Baranov, D. A. Zuev, S. I. Lepeshov, O. V. Kotov, A. E. Krasnok, A. B. Evlyukhin, and B. N. Chichkov, *Optica* **4**, 814 (2017).

[4] S. Liu, M. B. Sinclair, S. Saravi, G. A. Keeler, Y. Yang, J. Reno, G. M. Peake, F. Setzpfandt, I. Staude, T. Pertsch, and I. Brener, *Nano Lett.* **16**, 5426–5432 (2016).

[5] R. S. Savelev, D. S. Filonov, P. V. Kapitanova, A. E. Krasnok, A. E. Miroshnichenko, P. A. Belov, and Y. S. Kivshar, *Appl. Phys. Lett.* **105**, (2014).

[6] R. M. Bakker, Y. F. Yu, R. Paniagua-Domínguez, B. Luk'yanchuk, and A. I. Kuznetsov, *Nano Lett.* **17**, 3458–3464 (2017).

[7] Y. H. Fu, A. I. Kuznetsov, A. E. Miroshnichenko, Y. F. Yu, and B. Luk'yanchuk, *Nat. Commun.* **4**, 1527 (2013).

[8] K. Chen, Y. Feng, F. Monticone, J. Zhao, B. Zhu, T. Jiang, L. Zhang, Y. Kim, X. Ding, S. Zhang, A. Alù, and C. W. Qiu, *Adv. Mater.* **29**, 1–7 (2017).

[9] K. Koshelev, S. Kruk, E. Melik-Gaykazyan, J. H. Choi, A. Bogdanov, H. G. Park, and Y.

Kivshar, *Science (80-.).* **367**, 288–292 (2020).

[10] A. S. Shalin, *Quantum Electron.* **40**, 1004–1011 (2010).

[11] P. M. Voroshilov, C. R. Simovski, P. A. Belov, and A. S. Shalin, *J. Appl. Phys.* **117**, (2015).

[12] Y. Cui, D. van Dam, S. A. Mann, N. J. J. van Hoof, P. J. van Veldhoven, E. C. Garnett, E. P. A. M. Bakkers, and J. E. M. Haverkort, *Nano Lett.* **16**, 6467–6471 (2016).

[13] P. D. Terekhov, K. V. Baryshnikova, Y. Greenberg, Y. H. Fu, A. B. Evlyukhin, A. S. Shalin, and A. Karabchevsky, *Sci. Rep.* **9**, 3438 (2019).

[14] J. Algorri, D. Zografopoulos, A. Ferraro, B. García-Cámara, R. Vergaz, R. Beccherelli, and J. Sánchez-Pena, *Nanomaterials* **9**, 30 (2018).

[15] S. Jahani, and Z. Jacob, *Nat. Nanotechnol.* **11**, 23–36 (2016).

[16] H. K. Shamkhi, K. V. Baryshnikova, A. Sayanskiy, P. Kapitanova, P. D. Terekhov, P. Belov, A. Karabchevsky, A. B. Evlyukhin, Y. Kivshar, and A. S. Shalin, *Phys. Rev. Lett.* **122**, 193905 (2019).

[17] D. Wang, Q. Fan, J. Wang, Z. Zhang, Y. Liang, and T. Xu, *Guangdian Gongcheng/Opto-Electronic Eng.* **44**, 103–107 (2017).

[18] A. Canós Valero, D. Kislov, E. A. Gurvitz, H. K. Shamkhi, A. A. Pavlov, D. Redka, S. Yankin, P. Zemánek, and A. S. Shalin, *Adv. Sci.* **7**, 1903049 (2020).

[19] P. Grahn, A. Shevchenko, and M. Kaivola, *New J. Phys.* **14**, (2012).

[20] R. Alaee, C. Rockstuhl, and I. Fernandez-Corbaton, *Opt. Commun.* **407**, 17–21 (2018).

[21] A. B. Evlyukhin, T. Fischer, C. Reinhardt, and B. N. Chichkov, *Phys. Rev. B* **94**, 1–7 (2016).

[22] R. E. Raab, and O. L. Lange, Multipole Theory in Electromagnetism (Oxford Science Publications, New York, n.d.).

[23] J. D. Jackson, Classical Electrodynamics, 3rd ed. (New York, {NY}, 1999).

[24] N. Papasimakis, V. A. Fedotov, V. Savinov, T. A. Raybould, and N. I. Zheludev, *Nat. Mater.* **15**, 263–271 (2016).

[25] V. M. Dubovik, and V. V. Tugushev, *Phys. Rep.* **187**, 145–202 (1990).

[26] A. T. Góngora, and E. Ley-Koo, *Rev. Mex. Fis. E* **52**, 188–197 (2006).

[27] V. A. Fedotov, A. V. Rogacheva, V. Savinov, D. P. Tsai, and N. I. Zheludev, *Sci. Rep.* **3**, 1–5 (2013).

[28] N. A. Nemkov, A. A. Basharin, and V. A. Fedotov, *Phys. Rev. A* **98**, 1–9 (2018).

[29] E. A. Gurvitz, K. S. Ladutenko, P. A. Dergachev, A. B. Evlyukhin, A. E. Miroshnichenko, and A. S. Shalin, *Laser Photon. Rev.* **13**, 1800266 (2019).

[30] J. S. Totero Gongora, A. E. Miroshnichenko, Y. S. Kivshar, and A. Fratalocchi, *Nat. Commun.* **8**, 15535 (2017).

[31] A. A. Basharin, V. Chuguevsky, N. Volsky, M. Kafesaki, and E. N. Economou, *Phys. Rev. B* **95**, 1–10 (2017).

[32] T. Xiang, T. Lei, X. Huang, Z. Shen, and H. Yang, *Appl. Phys. Express* **11**, 2–5 (2018).

[33] P. D. Terekhov, K. V. Baryshnikova, A. S. Shalin, A. Karabchevsky, and A. B. Evlyukhin, *Opt. Lett.* **42**, 835 (2017).

[34] A. E. Miroshnichenko, A. B. Evlyukhin, Y. F. Yu, R. M. Bakker, A. Chipouline, A. I. Kuznetsov, B. Luk'yanchuk, B. N. Chichkov, and Y. S. Kivshar, *Nat. Commun.* **6**, 1–8 (2015).

[35] K. Baryshnikova, D. Filonov, C. Simovski, A. Evlyukhin, A. Kadochkin, E. Nenasheva, P. Ginzburg, and A. S. Shalin, *Phys. Rev. B* **98**, 1–9 (2018).

[36] L. Hüttenhofer, F. Eckmann, A. Lauri, J. Cambiasso, E. Pensa, Y. Li, E. Cortés, I. D. Sharp, and S. A. Maier, *ACS Nano* **14**, 2456–2464 (2020).

[37] D. G. Baranov, R. Verre, P. Karpinski, and M. Käll, *ACS Photonics* **5**, 2730–2736 (2018).

[38] R. Verre, D. G. Baranov, B. Munkhbat, J. Cuadra, M. Käll, and T. Shegai, *Nat. Nanotechnol.* **14**, 679–684 (2019).

[39] L. Xu, M. Rahmani, K. Zangeneh Kamali, A. Lamprianidis, L. Ghirardini, J. Sautter, R. Camacho-Morales, H. Chen, M. Parry, I. Staude, G. Zhang, D. Neshev, and A. E. Miroshnichenko, *Light Sci. Appl.* **7**, 44 (2018).

[40] G. Grinblat, Y. Li, M. P. Nielsen, R. F. Oulton, and S. A. Maier, *Nano Lett.* **16**, 4635–4640 (2016).

[41] T. Shibanuma, G. Grinblat, P. Albella, and S. A. Maier, *Nano Lett.* **17**, 2647–2651 (2017).

[42] S. V. Makarov, M. I. Petrov, U. Zywietz, V. Milichko, D. Zuev, N. Lopanitsyna, A. Kuksin, I. Mukhin, G. Zograf, E. Ubyivovk, D. A. Smirnova, S. Starikov, B. N. Chichkov, and Y. S. Kivshar, *Nano Lett.* **17**, 3047–3053 (2017).

[43] A. Kaldun, A. Blättermann, V. Stooß, S. Donsa, H. Wei, R. Pazourek, S. Nagele, C. Ott, C. D. Lin, J. Burgdörfer, and T. Pfeifer, *Science (80-.).* **354**, 738–741 (2016).

[44] S. Lepeshov, and A. Krasnok, *Optica* **7**, 1024 (2020).

[45] W. Liu, B. Lei, J. Shi, H. Hu, and A. E. Miroshnichenko, *J. Nanomater.* **2015**, 382 (2015).

[46] W. Liu, J. Zhang, B. Lei, H. Hu, and A. E. Miroshnichenko, *Opt. Lett.* **40**, 2293 (2015).

[47] J. Tian, H. Luo, Y. Yang, F. Ding, Y. Qu, D. Zhao, M. Qiu, and S. I. Bozhevolnyi, *Nat. Commun.* **10**, 1–9 (2019).

[48] A. K. Ospanova, I. V. Stenishchev, and A. A. Basharin, *Laser Photon. Rev.* **12**, 1800005 (2018).

[49] S. A. Maier, M. P. Nielsen, G. Grinblat, Y. Li, and R. F. Oulton, *ACS Nano* **11**, 953–960 (2016).

[50] Z.-J. Yang, Y.-H. Deng, Y. Yu, and J. He, *Nanoscale* **12**, 10639–10646 (2020).

[51] B. Luk'yanchuk, R. Paniagua-Domínguez, A. I. Kuznetsov, A. E. Miroshnichenko, and Y. S. Kivshar, *Phys. Rev. A* **95**, 1–8 (2017).

[52] A. K. Ospanova, A. Basharin, A. E. Miroshnichenko, and B. Luk'yanchuk, *Opt. Mater. Express* **11**, 23 (2021).

[53] E. A. Gurvitz, K. S. Ladutenko, P. A. Dergachev, A. B. Evlyukhin, A. E. Miroshnichenko, and A. S. Shalin, *Laser Photonics Rev.* **13**, 1800266 (2019).

[54] W. Yan, R. Faggiani, and P. Lalanne, *Phys. Rev. B* **97**, 205422 (2018).

[55] P. Lalanne, W. Yan, K. Vynck, C. Sauvan, and J. P. Hugonin, *Laser Photonics Rev.* **12**, 1–38 (2018).

[56] M. I. Tribelsky, and A. E. Miroshnichenko, *Phys. Rev. A* **100**, 1–5 (2019).

[57] O. Ávalos-Ovando, L. V. Besteiro, Z. Wang, and A. O. Govorov, *ArXiv* **9**, 3587–3595 (2020).

[58] M. I. Tribelsky, and A. E. Miroshnichenko, *Phys. Rev. A* **93**, 053837 (2016).

[59] L. Wei, Z. Xi, N. Bhattacharya, and H. P. Urbach, *Optica* **3**, 799 (2016).

[60] S. Gladyshev, K. Frizyuk, and A. Bogdanov, *Phys. Rev. B* **102**, 075103 (2020).

[61] E. Takou, A. C. Tasolamprou, O. Tsilipakos, and E. N. Economou, *Phys. Rev. B* **100**, 085431 (2019).

[62] J. A. Parker, H. Sugimoto, B. Coe, D. Eggena, M. Fujii, N. F. Scherer, S. K. Gray, and U. Manna, *Phys. Rev. Lett.* (2020).

[63] V. A. Zenin, S. M. Novikov, Y. Yang, B. N. Chichkov, S. I. Bozhevolnyi, A. B. Evlyukhin, R. Malureanu, and A. V Lavrinenko, *Nano Lett.* **17**, 7152–7159 (2017).

[64] K. Zhang, and D. Li, Electromagnetic Theory for Microwaves and Optoelectronics (Springer Berlin Heidelberg, Berlin, Heidelberg, 2008).

[65] M. I. Tribelsky, and A. E. Miroshnichenko, *Phys. Rev. A* **100**, 053824 (2019).

[66] M. F. Limonov, M. V. Rybin, A. N. Poddubny, and Y. S. Kivshar, *Nat. Photonics* **11**, 543–554 (2017).

[67] B. Hopkins, A. N. Poddubny, A. E. Miroshnichenko, and Y. S. Kivshar, *Phys. Rev. A* **88**, 053819 (2013).

[68] Y. Yang, A. E. Miroshnichenko, S. V. Kostinski, M. Odit, P. Kapitanova, M. Qiu, and Y. S. Kivshar, *Phys. Rev. B* **95**, 165426 (2017).

[69] A. A. Bogdanov, K. L. Koshelev, P. V. Kapitanova, M. V. Rybin, S. A. Gladyshev, Z. F. Sadrieva, K. B. Samusev, Y. S. Kivshar, and M. F. Limonov, *Adv. Photonics* **1**, 1 (2019).

[70] R. F. Harrington, Time-Harmonic Electromagnetic Fields (Wiley, 2001).

[71] C. Gigli, T. Wu, G. Marino, A. Borne, G. Leo, and P. Lalanne, *ACS Photonics* acsphotonics.0c00014 (2020).

[72] Y. Qin, B. Ji, X. Song, and J. Lin, *Appl. Phys. B Lasers Opt.* **125**, 1–8 (2019).

[73] J. Kim, E. G. Carnemolla, C. DeVault, A. M. Shaltout, D. Faccio, V. M. Shalaev, A. V. Kildishev, M. Ferrera, and A. Boltasseva, *Nano Lett.* (2018).

[74] S. E. Svyakhovskiy, V. V. Ternovski, and M. I. Tribelsky, *Opt. Express* **27**, 23894 (2019).

[75] N. Maccaferri, S. Meuret, N. Kornienko, and D. Jariwala, *Nano Lett.* (2020).

[76] M. Zhang, C. Wang, Y. Hu, A. Shams-Ansari, T. Ren, S. Fan, and M. Lončar, *Nat. Photonics* (2019).

[77] B. Vial, F. Zolla, A. Nicolet, and M. Commandré, *Phys. Rev. A - At. Mol. Opt. Phys.* **89**, 1–15 (2014).

[78] A. I. Kuznetsov, A. E. Miroshnichenko, M. L. Brongersma, Y. S. Kivshar, and B. Luk'yanchuk, *Science (80-.).* **354**, (2016).

[79] H. T. Chen, A. J. Taylor, and N. Yu, *Reports Prog. Phys.* **79**, (2016).

[80] P. D. Terekhov, V. E. Babicheva, K. V Baryshnikova, A. S. Shalin, A. Karabchevsky, and A. B. Evlyukhin, *Phys. Rev. B* **99**, 45424 (2019).

[81] F. J. García de Abajo, *Rev. Mod. Phys.* **79**, 1267–1290 (2007).

[82] A. M. Shaltout, V. M. Shalaev, and M. L. Brongersma, *Science (80-.).* **364**, eaat3100 (2019).

[83] S. Lepeshov, A. Krasnok, and A. Alù, *ACS Photonics* **6**, 2126–2132 (2019).

[84] M. Z. Alam, I. De Leon, and R. W. Boyd, *Science (80-.).* **352**, 795–797 (2016).

[85] Y. W. Huang, H. W. H. Lee, R. Sokhoyan, R. A. Pala, K. Thyagarajan, S. Han, D. P. Tsai, and H. A. Atwater, *Nano Lett.* **16**, 5319–5325 (2016).

[86] X.-Y. Xu, X.-L. Huang, Z.-M. Li, J. Gao, Z.-Q. Jiao, Y. Wang, R.-J. Ren, H. P. Zhang, and X.-M. Jin, *Sci. Adv.* **6**, eaay5853 (2020).